ELECTROCHEMISTRY

# Thermal batteries based on inverse barocaloric effects

**Zhe Zhang[1,2]†, Kuo Li[3]†, Shangchao Lin[4]†*, Ruiqi Song[1], Dehong Yu[5], Yida Wang[3], Jingfan Wang[6], Shogo Kawaguchi[7], Zhao Zhang[1,2], Chenyang Yu[1,2], Xiaodong Li[8], Jie Chen[9], Lunhua He[9,10,11], Richard Mole[5], Bao Yuan[8,9], Qingyong Ren[8,9], Kun Qian[4], Zhuangli Cai[4], Jingui Yu[12], Mingchao Wang[13], Changying Zhao[4], Xin Tong[8,9], Zhidong Zhang[1,2]*, Bing Li[1,2]***

**To harvest and reuse low-temperature waste heat, we propose and realize an emergent concept—barocaloric thermal batteries based on the large inverse barocaloric effect of ammonium thiocyanate ($NH_4SCN$). Thermal charging is initialized upon pressurization through an order-to-disorder phase transition, and the discharging of 43 J $g^{-1}$ takes place at depressurization, which is 11 times more than the input mechanical energy. The thermodynamic equilibrium nature of the pressure-restrained heat-carrying phase guarantees stable long-duration storage. The barocaloric thermal batteries reinforced by their solid microscopic mechanism are expected to substantially advance the ability to take advantage of waste heat.**



## INTRODUCTION

Even if roughly 90% of the world's energy use today involves heat over a wide range of temperatures, the current ability to manipulate heat is still limited (*1*–*4*). The production of heat accounts for more than 50% of global final energy consumption (*5*), while the waste heat potential analysis reveals that 72% of the global primary energy consumption is lost after conversion mainly in the form of heat (*6*). Among the waste heat spectrum, 63% is below 100°C (*6*). The preferred strategy for thermal energy recycling is that low-temperature waste heat is stored after harvesting and reused for heating purposes without further conversion. Toward such a goal, great obstacles have to be overcome to improve the controllability and tunability of thermal energy (*7*, *8*).

Inspired by the recent discovery of colossal barocaloric effects (BCEs) in plastic crystals (*9*), we propose a thermal battery based on inverse BCEs as an emergent solution. Plastic crystals are also known as orientation-disordered crystals where huge entropy changes are obtained at the order-to-disorder transitions (*10*). As the transitions are effectively tuned by external pressures, they are promising candidate working materials for solid-state refrigeration (*9*). Unlike the normal barocaloric materials that release heat at pressurization, a material with an inverse BCE absorbs heat, in analogy to the pressure-induced ice melting (*11*). This uniqueness allows us to design a thermal battery, as schematically shown in Fig. 1A. The material is thermally charged through a pressure-induced order-to-disorder transition. At the same time, the heat sink contacting the material is cooled down. As long as the pressure is held, the material is equilibrated at the disordered state, for which the long-duration heat storage becomes feasible. This equilibrium state feature differs from the intrinsic metastability of other heat storage materials (*12*, *13*). The stored heat can be readily released at the transition back to the ordered state at depressurization, and then recharging can be followed. In the present study, we materialize this concept in $NH_4SCN$, which is the first compound exhibiting an inverse BCE with entropy changes above 100 J $kg^{-1}$ $K^{-1}$. Taking advantage of neutron scattering and complementary multiscale simulations, we have established the mechanism in depth. As an emergent solution to manipulate heat, barocaloric thermal batteries are expected to play an active role in plenty of applications such as low-temperature industrial waste heat harvesting and reuse, heat transfer systems of solid-state refrigeration, smart grid, and residential heat management.

## RESULTS

### Realization of barocaloric thermal batteries

The actual working processes of barocaloric thermal batteries are demonstrated in $NH_4SCN$. As shown in Fig. 1B, the temperature-pressure cycle is depicted by the dashed lines on the phase diagram. As shown in the corresponding heat flow data (Fig. 1C), the compound absorbs heat during pressurization and releases heat during depressurization. The latent heat of 43 J $g^{-1}$ at discharging is well consistent with that at charging. More thermal charging and discharging processes have also been repeated at different temperatures as included in fig. S1. The practical performances of barocaloric thermal batteries are further exploited at room temperature through the direct measurements of the temperature changes (figs. S2 to S4 and movie S1) in response to the applied pressures up to 300 MPa. Figure 1D shows the pressure-induced temperature changes ($\Delta T$) at pressure ramping rates of 10 MPa $s^{-1}$, and a rise of

[1]Shenyang National Laboratory for Materials Science, Institute of Metal Research, Chinese Academy of Sciences, 72 Wenhua Road, Shenyang, Liaoning 110016, China. [2]School of Materials Science and Engineering, University of Science and Technology of China, 72 Wenhua Road, Shenyang, Liaoning 110016, China. [3]Center for High Pressure Science and Technology Advanced Research, Beijing 100193, China. [4]Key Laboratory for Power Machinery and Engineering of Ministry of Education, Institute of Engineering Thermophysics, School of Mechanical Engineering, Shanghai Jiao Tong University, Shanghai 200240, China. [5]Australian Nuclear Science and Technology Organisation, Locked Bag 2001, Kirrawee DC, NSW 2232, Australia. [6]Department of Mechanical Engineering, Florida State University, Tallahassee, FL 32310, USA. [7]Japan Synchrotron Radiation Research Institute, SPring-8, 1-1-1 Kouto, Sayo-cho, Sayo-gun, Hyogo 679-5198, Japan. [8]Institute of High Energy Physics, Chinese Academy of Sciences, Beijing 100049, China. [9]Spallation Neutron Source Science Center, Dongguan 523803, China. [10]Beijing National Laboratory for Condensed Matter Physics, Institute of Physics, Chinese Academy of Sciences, Beijing 100190, China. [11]Songshan Lake Materials Laboratory, Dongguan 523808, China. [12]School of Mechanical and Electronic Engineering, Wuhan University of Technology, Wuhan 430070, China. [13]Centre for Theoretical and Computational Molecular Science, Australian Institute for Bioengineering and Nanotechnology, The University of Queensland, St. Lucia, QLD 4072, Australia.
*Corresponding author. Email: bingli@imr.ac.cn (B.L.); zdzhang@imr.ac.cn (Z.Z.); shangchaolin@sjtu.edu.cn (S.L.)
†These authors contributed equally to this work.

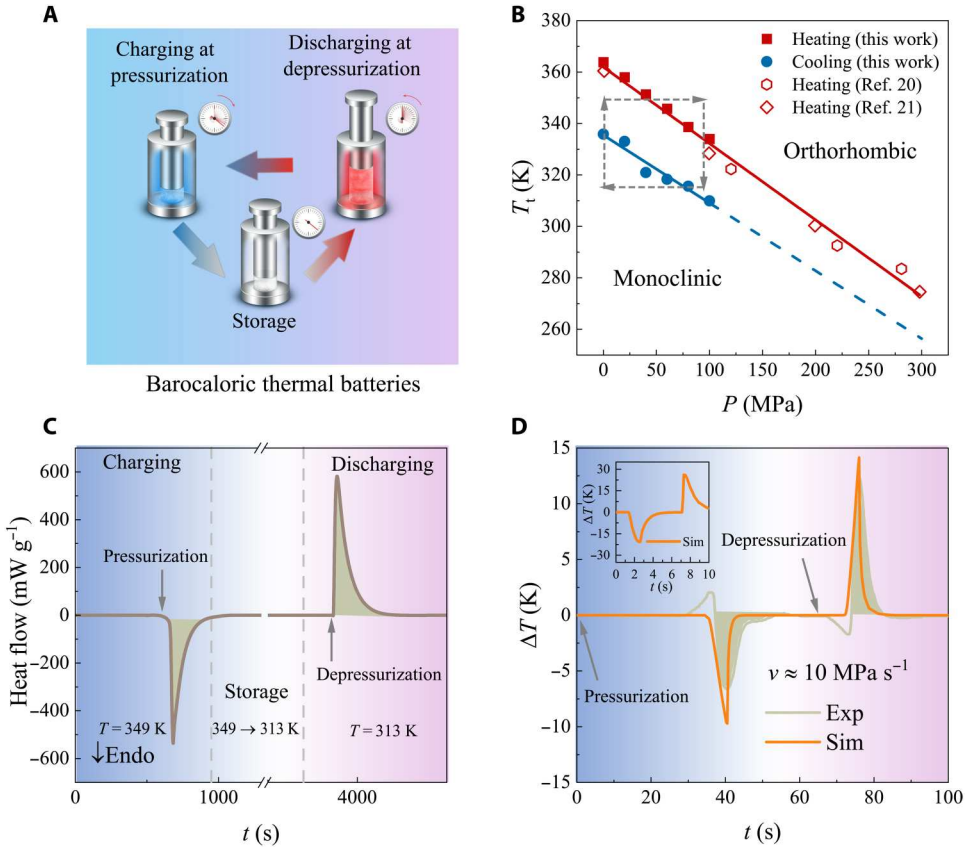


**Fig. 1. Barocaloric thermal batteries: Concept and realization.** (**A**) Schematic diagram for barocaloric thermal batteries including thermal charging at pressurization, storage, and thermal discharging at depressurization. (**B**) Phase diagram defined by the relationship between the transition temperature ($T_t$) and applied pressures (*20*, *21*). The dashed lines describe a complete process for barocaloric thermal batteries. (**C**) Heat flow variations as a function of time for a barocaloric thermal battery process [dashed lines in (B)] obtained on $NH_4SCN$ in the experiment at pressures changing between 8.2 and 90 MPa. The moments for applying and releasing pressures are arrowed. The temperature and pressure profiles are shown in fig. S1E. (**D**) Experimental and simulated relative temperature change ($\Delta T$) during charging (0.1 to 300 MPa) and discharging (300 to 0.1 MPa) at a ramping rate of 10 MPa s$^{-1}$. The inset shows the simulated process at extremely fast pressure ramping, leading to a maximum $\Delta T$ of about 26 K. Temperature changes are also recorded in movies S1 and S2.

12 K is found at discharging. The simulated process (see Materials and Methods and table S1) with a greatly short thermal exchange period indicates that theoretical $\Delta T$ is as high as 26 K (inset of Fig. 1D and movie S2). More repeats are shown in fig. S1 (C and D). Note that there is thermal hysteresis in the phase diagram, which is detrimental to refrigeration applications but beneficial to barocaloric thermal batteries given that under a given pressure, the larger thermal hysteresis, the larger working temperature span.

While we demonstrate heat harvesting and reuse under the control of external pressure above, it is crucial to reveal the physical origin of such a functionality for further improvement toward large-scale practical applications. What makes the barocaloric thermal batteries feasible is the inverse BCE of $NH_4SCN$. This compound has unique barocaloric performances not only because it is the first example bearing an inverse BCE but also because its large entropy changes accommodate the large relative cooling power (RCP). The maximum entropy changes ($\Delta S^{max}_{P_0 \to P}$) are about 128.7 J kg$^{-1}$ K$^{-1}$ (Fig. 2A) and are one order of magnitude larger than those of other current inverse barocaloric materials (Fig. 2B). The entropy changes at varying pressures indicate that the saturation pressure is about 80 MPa, in contrast to other systems whose saturation pressures are usually higher than 500 MPa (*14*–*19*). This leads to superior normalized entropy changes, $|\Delta S^{max}_{P_0 \to P}/P|$ = 1.61 J kg$^{-1}$ K$^{-1}$ MPa$^{-1}$. The phase transition temperature ($T_t$) is shifted to the lower temperatures at larger pressures. As shown in the *T*-*P* phase diagram (Fig. 1B) (*20*, *21*), at the pressure change from 0.1 to 100 MPa, $T_t$ (on heating) is shifted from 364 down to 334 K, giving rise to $|dT_t/dP|$ of about 0.3 K MPa$^{-1}$, which is also the largest as compared to other leading materials in Fig. 2C. For this reason, the obtained RCP is the largest as well (Fig. 2D). Compared to the previous reports (*16*) where a smaller $|dT_t/dP|$ leads to a larger entropy change and yet to a smaller RCP, the large entropy changes and RCP are simultaneously achieved in $NH_4SCN$ (fig. S5) because of the huge lattice volume changes to be described below.

As we point out in the introduction, the inverse BCE itself is considerably unique. To establish the full scenario on barocaloric thermal batteries, undoubtedly, it is necessary to clarify the atomic-level mechanism for the inverse BCE of $NH_4SCN$ at first. Therefore, we present the detailed crystal structures and atomic dynamics under both ambient pressure and applied pressures in the following sections, which provide a solid standing point to

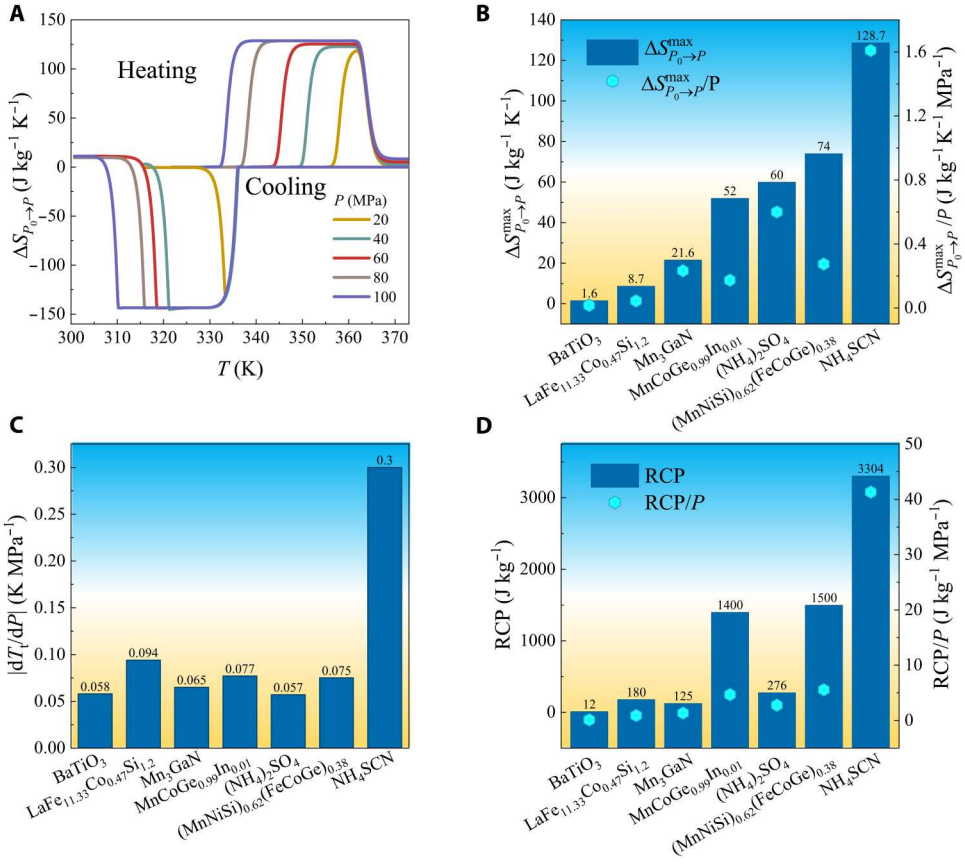


**Fig. 2. Large inverse BCE of $NH_4SCN$.** (**A**) Pressure-induced entropy changes ($\Delta S_{P_0 \to P}$) at pressure changing from $P_0$ = 0.1 MPa to $P$ = 20, 40, 60, 80, and 100 MPa. (**B**) Maxima of pressure-induced entropy changes ($\Delta S^{max}_{P_0 \to P}$) and normalized values by the driving pressure of $NH_4SCN$ compared with other leading materials with inverse BCEs. (**C**) $|dT_t/dP|$ for these materials. (**D**) RCP and normalized RCP.

discuss the physical origin of the inverse BCE and further the thermal battery.

## Crystal structures and atomic dynamics of $NH_4SCN$

Previous investigations suggest that $NH_4SCN$ undergoes successive phase transitions from monoclinic to orthorhombic, and further to tetragonal phases at about 360 and 390 K, respectively (*22*–*25*). The large inverse BCE is attributed to the former. Our neutron diffraction measurements on high-quality deuterated samples (fig. S6) confirm the crystal structures of the three phases (table S2), whose monoclinic-to-orthorhombic phase transition temperature is 358 K on heating. In the monoclinic phase, $ND_4^+$ and $SCN^-$ are both ordered (Fig. 3A). In particular, $SCN^-$ ions are oriented in an antiparallel fashion. As for the orthorhombic phase, D atoms in $ND_4^+$ ions become disordered (Fig. 3B), whose trajectories form a simple cubic lattice. In addition, the tetragonal phase is characteristic of the disordered $ND_4^+$ and $SCN^-$ ions (fig. S7A). Focusing on the former phase transition, we calculate the lattice dimensions as a function of temperature according to the synchrotron x-ray diffraction measurements (fig. S7, B to D). At the phase transition, the unit cell volume exhibits an abrupt contraction by about 5% (Fig. 3C), which corresponds to a giant specific volume change of about $-3.8 \times 10^{-5}$ $m^3$ $kg^{-1}$. This is just responsible for the combination of large $\Delta S^{max}_{P_0 \to P}$ and RCP because the huge volumetric change cancels the negative contribution of $|dT_t/dP|$ to entropy changes. In the orthorhombic phase, the $SCN^-$ ions are confined in the *ab* plane. At the orthorhombic-to-monoclinic transition, the $SCN^-$ ions tilt out of the *ab* plane to the *ac* plane, which leads to the increase of lattice constant *a* and *c*, corresponding to *b* and 2*a* in the monoclinic setting (fig. S7E). Such a negative thermal expansion is also confirmed in the predicted lattice constants of the monoclinic and orthorhombic phases (table S3) from both first-principle density functional theory (DFT) and molecular dynamics (MD) simulations (see Materials and Methods and tables S4 and S5). Negative thermal expansion behavior is intrinsically correlated to inverse BCE in terms of the thermodynamic relation $\left(\frac{\partial T}{\partial P}\right)_S = T\left(\frac{\partial V}{\partial T}\right)_P / C_P$, where $C_P$ is the specific heat (*26*).

Further, the atomic dynamics including both the reorientation dynamics and collective dynamics (phonons) are explored using quasi-elastic neutron scattering (QENS) and inelastic neutron scattering (INS), respectively. The elastic line signals of QENS spectra become broad, with temperature increasing (fig. S8, A to C). According to the fitting results at $Q$ = 1.2 $Å^{-1}$ (fig. S8, D to F), the spectra at 380 and 400 K are almost identical, and the QENS intensity is much stronger than that of 300 K. Therefore, the monoclinic-to-orthorhombic phase transition is accompanied by modifications of the reorientation dynamics of $NH_4^+$, whereas the orthorhombic-to-tetragonal one is not. Furthermore, elastic incoherent scattering factor (EISF) for $NH_4SCN$ is used to evaluate the reorientation

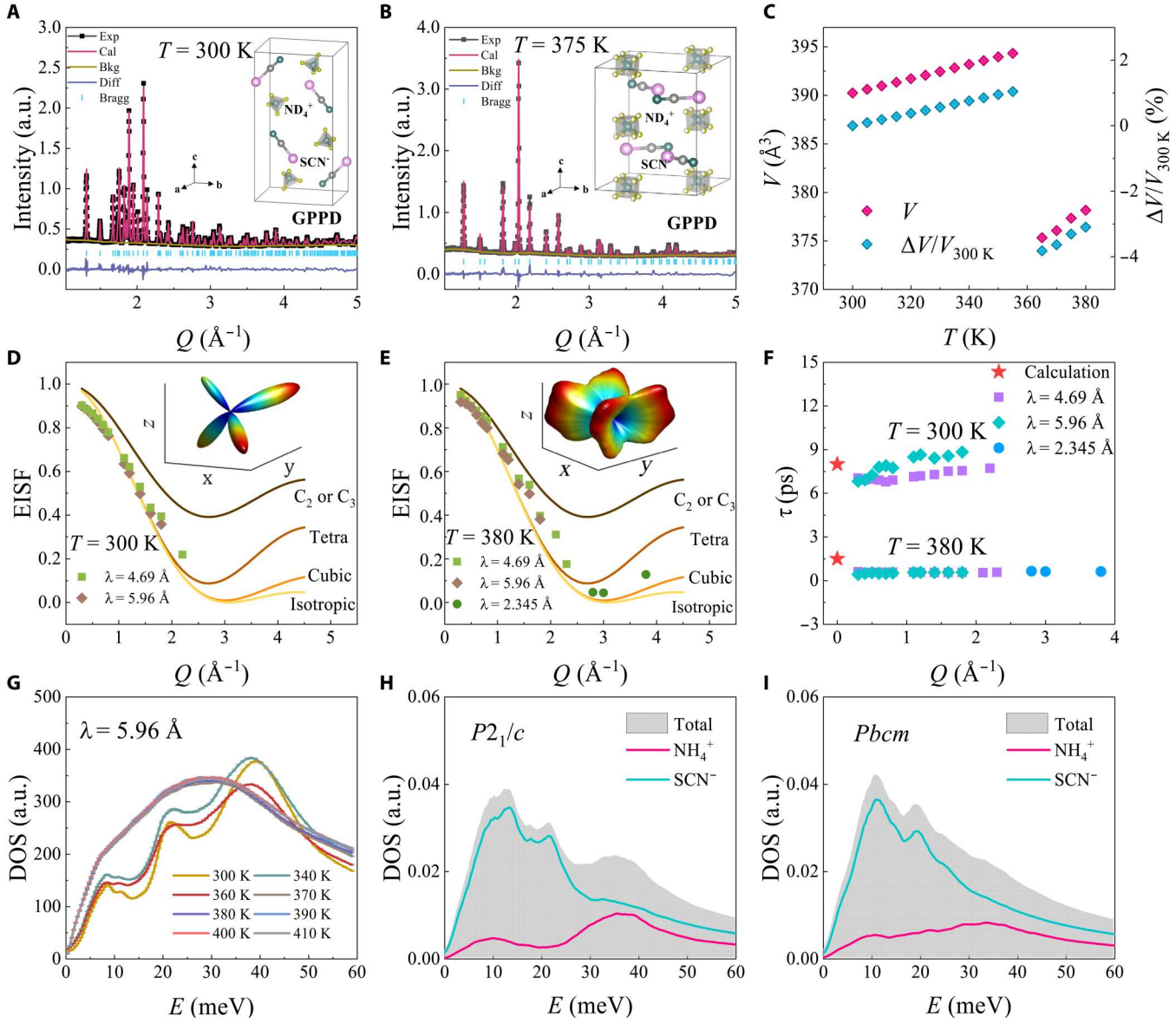


**Fig. 3. Crystal structures and atomic dynamics under ambient pressure.** (**A** and **B**) Rietveld refinements of the neutron powder diffraction patterns of $ND_4SCN$ at 300 K based on the $P2_1/c$ model and at 375 K based on the *Pbcm* model (in the insets). For the fitting, $R_{wp}$ = 3.41%, $R_p$ = 2.77%, and goodness of fit (GOF) = 4.57; $R_{wp}$ = 3.89%, $R_p$ = 3.02%, and GOF = 5.16, respectively. The detailed structural parameters determined in the refinements are listed in table S2. (**C**) Unit cell volume and its relative change as a function of temperature determined on the basis of synchrotron x-ray diffraction data (fig. S7). (**D** and **E**) Experimental EISF compared to a few models at 300 and 380 K, respectively. The insets are the spatial distribution of hydrogen atoms of $NH_4^+$ determined in MD simulations. (**F**) Experimental relaxation time (τ) compared to the MD simulations (fig. S9). (**G**) Experimental DOS up to 60 meV at different temperatures. (**H** and **I**) MD-predicted phonon DOS for $P2_1/c$ and *Pbcm* phases, respectively. a.u., arbitrary units.

dynamics. It can be seen that the 300-K data are close to the tetrahedral tumbling model (Fig. 3D), where the $NH_4^+$ tetrahedron is, as a whole, randomly oriented over four equivalent and undistinguishable configurations. Even if the high-$Q$ data were not accessed because of the limited $Q$ region of the instrument, this mode is supported by the crystal structure data as well as the MD-predicted orientational distribution contour plots (inset of Fig. 3D) and dynamic trajectories (fig. S9, C and E) of the N—H bonds of $NH_4^+$ in the monoclinic phase. As shown in Fig. 3E, the 380-K data are most likely described by the cubic tumbling mode even if a sizable deviation is present. Recalling the crystal structure, the orientation of the tetrahedron of $NH_4^+$ is random over a cubic lattice, which resembles the cubic tumbling model. However, it is clear that the experimental data points deviate from this model. More careful analysis of the crystal structure indicates that the hydrogen-bonding environment of $NH_4^+$ is not exactly symmetric. MD-predicted orientational surface plots (inset of Fig. 3E) and dynamic trajectories of the N—H bonds of $NH_4^+$ also suggest that such a cubic tumbling mode shows spatial preference (fig. S9, A, B, and D). As mentioned before, the QENS spectra of the orthorhombic phase

and the tetragonal phase are almost identical, which suggests that the motions of $NH_4^+$ at 400 K are the same. The average time scales (τ) show that the preferred cubic tumbling mode is much faster than the tetrahedral tumbling (Fig. 3F). The weak $Q$ dependence indicates the local nature of the modes. A weak $Q$ dependence has also been found in a similar system of $NaAlH_4$ (*27*). MD-predicted decoherence rates of $NH_4^+$ rotations (fig. S9, B to E) are in accordance with the experimentally estimated orientational relaxation times for both the monoclinic and orthorhombic phases (Fig. 3F).

We move to the collective atomic dynamics. The phonon density of state (DOS) of $NH_4SCN$ (Fig. 3G) shows that the strong peak at 40 meV is suppressed and broadened to be featureless above $T_t$. At the orthorhombic-to-tetragonal phase transition, however, the tetragonal phase exhibits an almost identical profile, similar to the situation of QENS. To understand such a temperature dependence, the MD simulations are performed to reproduce the phonon DOS (Fig. 3, H and I). It can be seen that the low-energy phonons are attributed to the motions of $SCN^-$, while the vibrations of $NH_4^+$ mostly appear around 40 meV. The structure of partial phonon DOS is well supported by the data of the deuterated sample shown in fig. S6, where the peak is softened from 40 to about 30 meV, indicative of its $NH_4^+$ origin. As for the orthorhombic phase, the partial phonon DOS of $NH_4^+$ is much more broadened than that of $SCN^-$. In addition, the peak at 40 meV is suppressed. These results are in good agreement with the experimental observations. In other words, the $NH_4^+$ vibrations are suppressed by the preferred cubic tumbling mode, which reflects the strong orientation-vibration coupling.

### Origin of the inverse BCE of $NH_4SCN$

We continue to explore the responses of the material to external pressures, to which the inverse BCE is directly related. Pressure-dependent synchrotron x-ray diffraction measurements indicate that the application of pressure (Fig. 4, A and B) induces a phase transition from monoclinic to orthorhombic phases at room temperature. Similarly, the pressure-dependent QENS measurements (Fig. 4C) indicate that there is a much wider QENS component superposed underneath the elastic peak at about 300 MPa as compared to the ambient pressure case. Thus, the in situ QENS measurements directly confirm the pressure-induced orientational disorder. As is known that atomic disorder is usually suppressed by pressure, the pressure-enhanced atomic disorder in $NH_4SCN$ is strikingly special. The pressure-induced phase transition can be well understood by the MD-predicted atomic dynamics. The gradual application of external pressure induces the localization of intense stress exclusively on $SCN^-$ ions (fig. S10). As atomic stress is a measure of instability of the system, the pressures tend to destabilize the monoclinic phase as manifested by the excited transverse vibrational mode of $SCN^-$ (Fig. 4D and fig. S11). The mean square displacement (MSD) reflecting the vibration amplitude exhibits a much more broadened probability distribution along the direction perpendicular to $SCN^-$ under 200 MPa. The transverse vibrations of $SCN^-$ have larger components along the hydrogen-bonding directions, as manifested in the angular distribution shown in Fig. 4 (E and F). Pressures promote these transverse vibrations, weaken the hydrogen-bonding network of the monoclinic phase, and eventually drive the phase transition to the more stable orthorhombic phase through tilting of $SCN^-$ and disordering of $NH_4^+$.

## DISCUSSION

Above, we have demonstrated and validated the barocaloric thermal batteries. Their realization does not only represent an emergent application of barocaloric materials beyond the conventional solid-state refrigeration but also brings an exciting prospect toward rational manipulation of thermal energy. Unlike other leading energy storage strategies such as chemical electric batteries (*28*) and hydrogen storage (*29*), thermal energy storage is usually subjected to inevitable spontaneous thermal dissipation, which prevents long-duration storage. In contrast, the pressure-induced thermodynamic equilibrium state ensures the long-duration stable storage of thermal energy. As far as efficiency is concerned, barocaloric thermal batteries are extraordinarily appealing. The input mechanical energy is estimated to be 3.85 J $g^{-1}$ by the product of the driving pressure and the induced volume changes of the material at the phase transition, whereas stored heat is about 43 J $g^{-1}$. At full discharging, the overall efficiency is about 92% if the energy input for discharging is ignored.

With the merits of high-efficiency and long-duration storage, three promising applications are specified (figs. S12 to S14). First, it is known that thermal transfer is a key issue for solid-state refrigeration technology. With a hybrid caloric refrigeration cycle involving a regular caloric material as a refrigeration working substance and a barocaloric thermal battery as a high-temperature heat sink, it is possible to accelerate the solid-state thermal transfer and eventually improve the overall efficiency. Second, in principle, pressurization needs specialized infrastructures, while depressurization is much easier. Thus, barocaloric thermal batteries are suitable for circumstances of centralized charging and distributed discharging. For instance, low-temperature waste heat at power plants and data centers can be well collected and stored for residential heating. It is also likely to manage solar thermal energy through a diurnal cycle for building thermal management. Last, barocaloric thermal batteries provide an alternative approach to solving the intermittency problem of solar and wind electricity. In the peak of supply, electricity can be converted into heat and stored for a flexible period. In particular, barocaloric thermal batteries can be incorporated into the current compressed air energy storage system, where thermal energy and mechanical energy are simultaneously stored. Note that, in thermodynamic analogy, such an idea of thermal batteries can be well translated to other types of caloric materials, for example, in electrocaloric compounds (*30*).

To summarize, the large inverse BCE has been discovered in $NH_4SCN$ with the simultaneously large $\Delta S^{max}_{P_0 \to P}$ and RCP. This unique property has been well understood, and the fundamental microscopic mechanism has been successfully established. Rooted in this effect, high-performance barocaloric thermal batteries are materialized, which are characteristic of long-duration stability and excellent tunability. The demonstrated barocaloric thermal batteries are expected to benefit rational energy utilization.

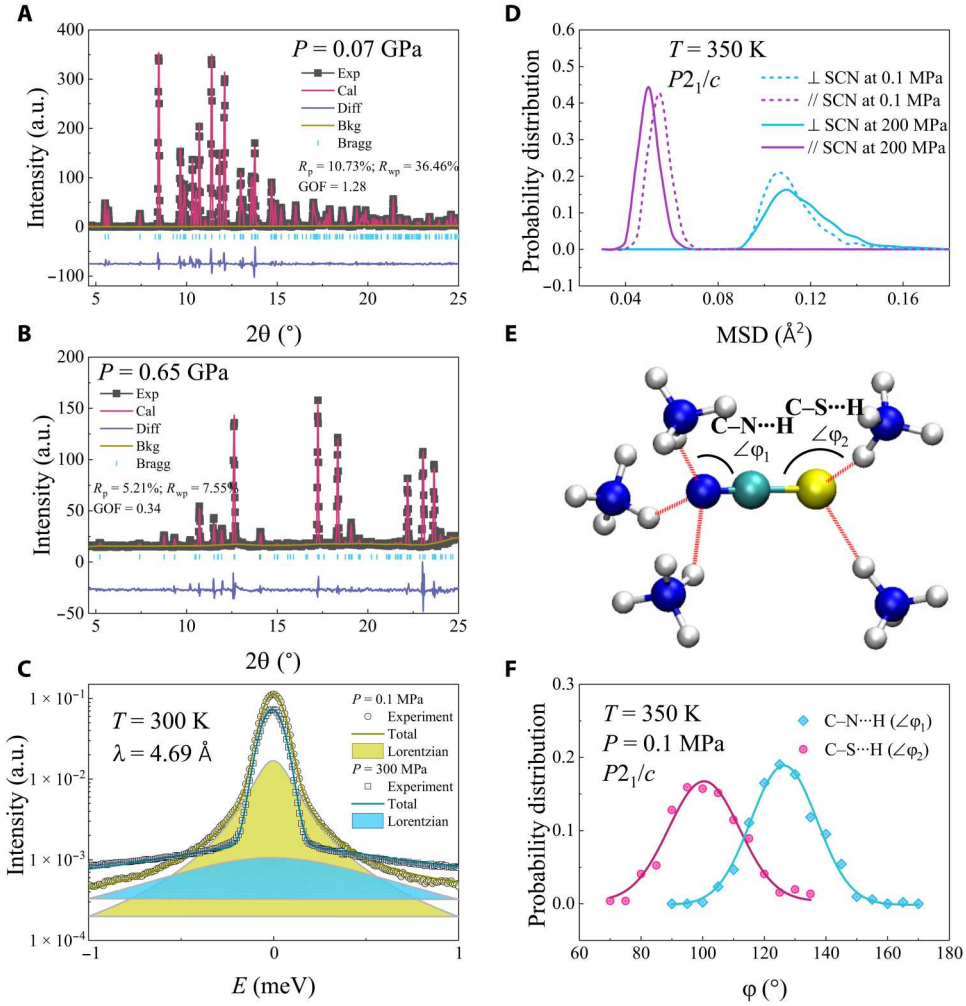


**Fig. 4. Structural and dynamics in response to external pressures.** (**A** and **B**) Synchrotron x-ray diffraction patterns and refinements at room temperature under 0.07 and 0.65 GPa, respectively. (**C**) *Q*-integrated QENS spectra at room temperature under ambient pressure and 300 MPa. The Lorentzian components are highlighted as shaded regions. (**D**) Probability distribution of MSD (amplitude of atomic vibrations) decomposed into the directions perpendicular to and parallel with $SCN^-$ vectors in the $P2_1/c$ model under ambient pressure and 200 MPa at 350 K. (**E**) Illustration of C—N···H and C—S···H hydrogen bonds, whose angles with respect to the $SCN^-$ vector are labeled as $\varphi_1$ and $\varphi_2$, respectively. (**F**) Probability distribution of angles $\varphi_1$ and $\varphi_2$. The solid lines represent fits to Gaussian functions, giving rise to peaks at 100.5(6)° and 126.4(3)°.

## MATERIALS AND METHODS

### Samples

$NH_4SCN$ (purity 99.99%) was purchased from Aladdin. $ND_4SCN$ was prepared by replacing H with D in an aqueous solution of $NH_4SCN$ in $D_2O$. Five grams of $NH_4SCN$ was dissolved completely in 30 ml of $D_2O$. After keeping static for 20 min, $H_2O$ and redundant $D_2O$ were removed using a rotary evaporator. The product was dried at 333 K for 6 hours under a vacuum. Such procedures were repeated several times to improve the purity. The quality of the products was confirmed by x-ray diffraction, high-pressure differential scanning calorimetry, and Raman scattering (fig. S6). All the samples were kept in a glove box and dehydrated for 1 hour at a temperature of 348 K before all the relevant experimental measurements.

### Pressure-induced temperature changes

The pressure-induced temperature changes at room temperature were measured on a VX3 Paris-Edinburgh press device with a K-typed thermocouple. $NH_4SCN$ powder samples weighted about 120 mg were pre-pressed into two hemispheres, where the thermocouple was sandwiched, and then they were placed onto the double-toroidal tungsten carbide anvils. An automatic hydraulic oil syringe pump was used to control the pressurization and depressurization processes at 2.5, 5, and 10 MPa $s^{-1}$. The maximum pressure was up to 300 MPa. NaCl was also measured as a reference. For more details, please refer to figs. S2 to S4 and movie S1.

### Pressure-dependent calorimetric characterizations

The heat flow data were collected as a function of temperature and pressure using a high-pressure differential scanning calorimeter (μDSC7, Setaram). The sample was enclosed in a high-pressure vessel made of Hastelloy. Hydrostatic pressure up to 100 MPa was

achieved by compressing nitrogen gas and accurately controlled by a high-pressure panel. Constant pressure scans were performed on $NH_4SCN$ at 0.1, 20, 40, 60, 80, and 100 MPa at a rate of 1 K $min^{-1}$, respectively. Heat flow data after subtracting baseline background were converted to entropy changes, as described before (*9*). RCP was obtained as follows (*31*)

$$\mathrm{RCP} = \Delta S^{\max}_{P_0 \to P} \cdot \delta T_{\mathrm{FWHM}} \quad (1)$$

where $\delta T_{\mathrm{FWHM}}$ is the full width at half maximum for $\Delta S^{\max}_{P_0 \to P}$ as a function of temperature. For the constant temperature process, the samples of $NH_4SCN$ were pressurized from 8.2 to 90 MPa at 345, 349, and 355 K and depressurized back to 8.2 MPa at 318, 313, and 315 K, respectively. Under the same conditions, the signals of an empty cell were obtained and subtracted as background.

### Neutron powder diffraction

Neutron powder diffraction experiments were performed on $ND_4SCN$ at the general purpose powder diffractometer (*32*) of China Spallation Neutron Source (CSNS) in China. The powder amount of 0.57 g was put into a vanadium can ($\phi$ = 9 mm; $L$ = 70 mm). Constant temperature scans were done at 300, 375, and 400 K, respectively. At each temperature, the counting persisted for 5 hours. The diffraction patterns were fitted on the basis of individual structural models (table S2) using Jana2006 software (*33*).

### Synchrotron x-ray diffraction

Ambient-pressure synchrotron x-ray diffraction was conducted at the beamline BL02B2 of SPring-8 in Japan (*34*). The x-ray wavelength was 0.999108 Å. A small amount of powder sample was sealed into a quartz capillary ($\phi$ = 0.5 mm). The diffraction data were obtained in a temperature region from room temperature up to 380 K. Each scan took about 3 min. The pressure-dependent diffraction data were obtained at the high-pressure beamline of the Beijing Synchrotron Radiation Facility (BSRF) in China. The standard sample of $CeO_2$ was used for calibration before the experiment. The powder sample was loaded into a diamond anvil cell to access pressure of 0.07 and 0.65 GPa at room temperature. The resulting data were analyzed by Le Bail fitting in Jana2006 software (*33*).

### INS and QENS

The INS and QENS experiments of $NH_4SCN$ and $ND_4SCN$ were conducted at the time-of-flight neutron spectrometer Pelican of Australian Center for Neutron Scattering of Australian Nuclear Science and Technology Organisation (ANSTO) in Australia (*35*). The instrument was configured for incident neutron wavelengths of 2.345, 4.69, and 5.96 Å, corresponding to incident energy of 14.9, 3.7, and 2.3 meV with resolutions of 0.7, 0.135, and 0.065 meV at the elastic lines, respectively. The dehydrated samples were sealed into aluminum cans under a helium gas environment. The experiments were performed in a temperature region from room temperature up to 410 K for $NH_4SCN$ and at 300 and 380 K for $ND_4SCN$. The pressure-dependent measurements were carried out at 0.1 and 300 MPa with an incident wavelength of 4.69 Å at 300 K using a high-pressure cell made of high-strength aluminum alloy. The background was corrected by the data of empty cans measured under the same conditions. The instrument resolution functions were obtained on a standard cylindrical vanadium tube at 300 K. The spectra of the vanadium standard were also used for detector normalization. The data reduction and processing were completed in the Large Array Manipulation Program (LAMP) software (*36*). The dynamic structure factor $S(Q, E)$, as a function of scattering wave vectors ($Q$) and energy transfer ($E$), was measured over a wide temperature range. The generalized phonon DOS was obtained using the formula

$$g(E) = \int \frac{E}{Q^2} S(Q,E)\left(1 - e^{-\frac{E}{k_B T}}\right) dQ \quad (2)$$

where $k_B$ is Boltzmann's constant and $T$ is temperature. The $S(Q, E)$ data were sliced at selected $Q$ points, where Bragg peaks were avoided. The sliced spectra were fitted in the PAN module of Data Analysis and Visualization Environment (DAVE) (*37*). One Lorentzian function, one delta function, and a linear background were used for the spectral fitting with wavelengths of 4.69 and 5.96 Å. One more damped harmonic oscillator function was added to fit the spectra with a wavelength of 2.345 Å because phonons were probed.

### DFT and MD simulations

We conducted DFT calculations using VASP (*38*, *39*) to determine the lattice parameters of $NH_4SCN$ of orthorhombic and monoclinic phases. The projector augmented wave (*40*) pseudopotentials and the generalized gradient approximation based on the Perdew-Burke-Ernzerhof (*41*) function were selected. Grimme's energy correction method was used to account for dispersion interactions (*42*). We selected a kinetic energy cutoff of 550 eV and the Γ-centered 6 × 6 × 4 Monkhorst-Pack (*43*) mesh for sampling as to minimize atomic forces below 1.0 meV $Å^{-1}$.

All-atomistic MD simulations were carried out using LAMMPS (*44*). The General AMBER Force Field with charges derived using the electrostatic-potential method force field (*45*, *46*) parameters was used. The time step was set to 1 fs, and a cutoff distance of 1 nm was chosen. The particle mesh Ewald summation method (*47*) was used here to treat long-range electrostatic interactions. All MD equilibrations of the initial structures were carried out for 2 ns under the *NPT* ensemble after energy minimization.

To provide transient information on reorientation dynamics of $NH_4^+$, we calculated the averaged cosine trajectory of N─H bonds, i.e., the angle spanned by the N─H bond vector as a function of time, $t$

$$\cos\theta_i(t - t_0) = \hat{n}_i(t) \cdot \hat{n}_i(t_0) \quad (3)$$

where $\hat{n}_i(t)$ is the unit vector for the N─H bond at any time $t$ and $\hat{n}_i(t_0)$ is that at the initial time $t_0$ = 20 ns. On the basis of the time needed for $\cos\theta_i(t - t_0)$ to decay to zero, we estimated the decoherent lifetime for $NH_4^+$ rotations (fig. S9).

The phonon DOS was computed for the orthorhombic and monoclinic phases of $NH_4SCN$ at their corresponding temperatures (350 and 300 K) and pressures (0.1 and 200 MPa). It was calculated by taking the Fourier transform of velocity autocorrelation function. Specifically (*48*),

$$D(\omega) = \int_0^{\tau} \left[ \sum_{i=1}^{N} m_i \frac{\langle v_i(t) \cdot v_i(0) \rangle}{\langle v_i(0) \cdot v_i(0) \rangle} \right] e^{-i\omega t} dt \quad (4)$$

where ω is the phonon angular frequency; $m_i$ is the mass of atom $i$; $v_i(t)$ and $v_i(0)$, respectively, are the velocities of atom $i$ at time $t$ and 0; and $N$ is the total number of atoms. To characterize the pressure-

induced changes in the transverse and longitudinal vibrational modes of $SCN^-$, the MSD functions of $SCN^-$ along the transverse (radial) and longitudinal (axial) directions of $SCN^-$ vector in a cylindrical coordinate were collected every 10 fs during a 1-ns MD simulation.

Using MD-predicted atomic trajectories, atomic von Mises stresses were computed to quantify the local stress. On the basis of the symmetric Cauchy stress tensor theory (*49*), the second invariant of the stress tensor is defined as the von Mises stress (*50*, *51*). The OVITO software package (*52*) is used to display local stress information.

### Finite Element (FE) thermal simulations

COMSOL Multiphysics platform (*53*) was used to stimulate the adiabatic temperature change based on a two-dimensional axisymmetric hemispherical geometric model with a diameter of $\phi = 6$ mm. The thermal and mechanical parameters of $NH_4SCN$ were summarized in table S1. In this model, the physical fields and corresponding several governing equations were described in a previous study (*54*). The boundary conditions in the solid-mechanics field were realized first by the function of pressure versus time (fig. S4). The ordinary differential equation (Eqs. 5 and 6) and boundary conditions of heat transfer in solids (Eq. 7) are shown below

$$\mathrm{Step}(P, T) + f = 1 \tag{5}$$

$$\mathrm{Step}(P, T) = \frac{1}{1 + e^{-\frac{100}{T_1 - T_2} \times [(T_1 - T_2) \times P - (P_1 - P_2) \times T - T_1 P_2 + T_2 P_1]}} \tag{6}$$

$$Q = -\mathrm{latent} \cdot \rho \cdot \left(-\frac{df}{dt}\right) \tag{7}$$

where latent represents the latent heat of the phase transition, i.e., 43 $J\,g^{-1}$; $P_1 = 20$ MPa; $P_2 = 0.1$ MPa; $T_1 = 358$ K; and $T_2 = 363.83$ K. The heat transfer coefficient $h$ at the thermal interface between the barocaloric material and the press die was set to be $5 \times 10^4$ $W\,m^{-2}\,K^{-1}$ for $\Delta T$ in Fig. 1D and fig. S1 (C and D).

## Supplementary Materials

**This PDF file includes:**

Figs. S1 to S14
Tables S1 to S5
Legends for movies S1 and S2
References

**Other Supplementary Material for this manuscript includes the following:**

Movies S1 and S2

## REFERENCES AND NOTES


1. I. Gur, K. Sawyer, R. Prasher, Searching for a better thermal battery. *Science* **335**, 1454–1455 (2012).
2. A. Henry, R. Prasher, A. Majumdar, Five thermal energy grand challenges for decarbonization. *Nat. Energy* **5**, 635–637 (2020).
3. Editorial, The Heat is on. *Nat. Energy* **1**, 16193 (2016).
4. G. P. Thiel, A. K. Stark, To decarbonize industry, we must decarbonize heat. *Joule* **5**, 531–550 (2021).
5. A. Eisentraut, A. Brown, "Heating without global warming" (Market Developments and Policy Considerations for Renewable Heat, 2014).
6. C. Forman, I. K. Muritala, R. Pardemann, B. Meyer, Estimating the global waste heat potential. *Renew. Sustain. Energy Rev.* **57**, 1568–1579 (2016).
7. G. G. D. Han, H. Li, J. C. Grossman, Optically-controlled long-term storage and release of thermal energy in phase-change materials. *Nat. Commun.* **8**, 1446 (2017).
8. N. H. S. Tay, M. Liu, M. Belusko, F. Bruno, Review on transportable phase change material in thermal energy storage systems. *Renew. Sustain. Energy Rev.* **75**, 264–277 (2017).
9. B. Li, Y. Kawakita, S. Ohira-Kawamura, T. Sugahara, H. Wang, J. Wang, Y. Chen, S. I. Kawaguchi, S. Kawaguchi, K. Ohara, K. Li, D. Yu, R. Mole, T. Hattori, T. Kikuchi, S. Yano, Z. Zhang, Z. Zhang, W. Ren, S. Lin, O. Sakata, K. Nakajima, Z. Zhang, Colossal barocaloric effects in plastic crystals. *Nature* **567**, 506–510 (2019).
10. N. G. Parsonage, L. A. K. Staveley, *Disorder in Crystals* (Clarendon Press, 1978).
11. L. D. Drake, R. L. Shreve, Pressure melting and regelation of ice by round wires. *Proc. R. Soc. Lond. A* **332**, 51–83 (1973).
12. B. Sandnes, J. Rekstad, Supercooling salt hydrates: Stored enthalpy as a function of temperature. *Sol. Energy* **80**, 616–625 (2006).
13. Y. Nakamura, Y. Sakai, M. Azuma, S. Ohkoshi, Long-term heat-storage ceramics absorbing thermal energy from hot water. *Sci. Adv.* **6**, eaaz5264 (2020).
14. E. Stern-Taulats, P. Lloveras, M. Barrio, E. Defay, M. Egilmez, A. Planes, J. L. Tamarit, L. Mañosa, N. D. Mathur, X. Moya, Inverse barocaloric effects in ferroelectric $BaTiO_3$ ceramics. *APL Mater.* **4**, 091102 (2016).
15. L. Mañosa, D. González-Alonso, A. Planes, M. Barrio, J. L. Tamarit, I. S. Titov, M. Acet, A. Bhattacharyya, S. Majumdar, Inverse barocaloric effect in the giant magnetocaloric La–Fe–Si–Co compound. *Nat. Commun.* **2**, 595 (2011).
16. D. Matsunami, A. Fujita, K. Takenaka, M. Kano, Giant barocaloric effect enhanced by the frustration of the antiferromagnetic phase in $Mn_3GaN$. *Nat. Mater.* **14**, 73–78 (2015).
17. R. R. Wu, L. F. Bao, F. X. Hu, H. Wu, Q. Z. Huang, J. Wang, X. L. Dong, G. N. Li, J. R. Sun, F. R. Shen, T. Y. Zhao, X. Q. Zheng, L. C. Wang, Y. Liu, W. L. Zuo, Y. Y. Zhao, M. Zhang, X. C. Wang, C. Q. Jin, G. H. Rao, X. F. Han, B. G. Shen, Giant barocaloric effect in hexagonal $Ni_2In$-type Mn-Co-Ge-In compounds around room temperature. *Sci. Rep.* **5**, 18027 (2015).
18. P. Lloveras, E. Stern-Taulats, M. Barrio, J. L. Tamarit, S. Crossley, W. Li, V. Pomjakushin, A. Planes, L. Mañosa, N. D. Mathur, X. Moya, Giant barocaloric effects at low pressure in ferrielectric ammonium sulphate. *Nat. Commun.* **6**, 8801 (2015).
19. T. Samanta, P. Lloveras, A. U. Saleheen, D. L. Lepkowski, E. Kramer, I. Dubenko, P. W. Adams, D. P. Young, M. Barrio, J. L. Tamarit, N. Ali, S. Stadler, Barocaloric and magnetocaloric effects in $(MnNiSi)_{1-x}(FeCoGe)_x$. *Appl. Phys. Lett.* **112**, 021907 (2018).
20. L. S. Smirnov, V. A. Goncharova, E. L. Gromnitskaya, G. G. Il'ina, I. Natkaniec, A. I. Solov'ev, O. V. Stal'gorova, The acoustic and neutron scattering investigations of $NH_4SCN$ phase diagram. *High Press. Res.* **13**, 65–70 (1994).
21. P. W. Bridgman, Polymorphic transformations of solids under pressure. *Proc. Am. Acad. Arts Sci.* **51**, 55–124 (1915).
22. A. Hamada, S. Yamamoto, Y. Shinnaka, Structural study of tetragonal-orthorhombic phase transition in $NH_4SCN$. *J. Phys. Soc. Jpn.* **59**, 954–958 (1990).
23. J. W. Bats, P. Coppens, The experimental charge distribution in sulfur-containing molecules. A study of the deformation density in $NH_4SCN$ at 81 K by combined x-ray and neutron diffraction. *Acta Crystallogr.* **33**, 1542–1548 (1977).
24. Y. Kinsho, N. Onodera, M. Sakiyama, S. Seki, Thermodynamic studies on phase transitions of potassium thiocyanate and ammonium thiocyanate crystals. *Bull. Chem. Soc. Jpn.* **52**, 395–402 (1979).
25. R. Blinc, J. Seliger, V. Žagar, T. Apih, J. Dolinšek, H. Warhanek, A. Fuith, W. Schranz, $^{14}N$ nuclear-quadrupole-resonance study of the structural phase transitions in $NH_4SCN$. *Phys. Rev. B* **42**, 8125 (1990).
26. R. K. Rajput, *Engineering Thermodynamics: A Computer Approach (SI Units Version)* (Jones & Bartlett Publishers, 2009).
27. S. NaraseGowda, C. M. Brown, M. Tyagi, T. Jenkins, T. A. Dobbins, Quasi-elastic neutron scattering studies of hydrogen dynamics for nanoconfined $NaAlH_4$. *J. Phys. Chem. C* **120**, 14863–14873 (2016).
28. B. Dunn, H. Kamath, J.-M. Tarascon, Electrical energy storage for the grid: A battery of choices. *Science* **334**, 928–935 (2011).
29. B. Sakintuna, F. Lamari-Darkrim, M. Hirscher, Metal hydride materials for solid hydrogen storage: A review. *Int. J. Hydrogen Energy* **32**, 1121–1140 (2007).
30. B. Peng, Q. Zhang, B. Gang, G. J. T. Leighton, C. Shaw, S. J. Milne, B. Zou, W. Sun, H. Huang, Z. Wang, Phase-transition induced giant negative electrocaloric effect in a lead-free relaxor ferroelectric thin film. *Energy Environ. Sci.* **12**, 1708–1717 (2019).
31. K. A. GschneidnerJr., V. K. Pecharsky, A. O. Tsokol, Recent developments in magnetocaloric materials. *Rep. Prog. Phys.* **68**, 1479 (2005).
32. J. Chen, L. Kang, H. Lu, P. Luo, F. Wang, H. He, The general purpose powder diffractometer at CSNS. *Phys. B Condens. Matter* **551**, 370–372 (2018).

33. V. Petříček, M. Dušek, L. Palatinus, Crystallographic computing system JANA2006: General features. *Z. Kristallogr. Cryst. Mater.* **229**, 345–352 (2014).
34. S. Kawaguchi, M. Takemoto, K. Osaka, E. Nishibori, C. Moriyoshi, Y. Kubota, Y. Kuroiwa, K. Sugimoto, High-throughput powder diffraction measurement system consisting of multiple MYTHEN detectors at beamline BL02B2 of SPring-8. *Rev. Sci. Instrum.* **88**, 085111 (2017).
35. D. Yu, R. Mole, T. Noakes, S. Kennedy, R. Robinson, Pelican—A time of flight cold neutron polarization analysis spectrometer at OPAL. *J. Phys. Soc. Jpn.* **82**, SA027 (2013).
36. D. Richard, M. Ferrand, G. J. Kearley, Analysis and visualisation of neutron-scattering data. *J. Neutron Res.* **4**, 33–39 (1996).
37. R. T. Azuah, L. R. Kneller, Y. Qiu, P. L. W. Tregenna-Piggott, C. M. Brown, J. R. D. Copley, R. M. Dimeo, DAVE: A comprehensive software suite for the reduction, visualization, and analysis of low energy neutron spectroscopic data. *J. Res. Natl. Inst. Stand. Technol.* **114**, 341–358 (2009).
38. G. Kresse, J. Furthmüller, Efficient iterative schemes for ab initio total-energy calculations using a plane-wave basis set. *Phys. Rev. B* **54**, 11169 (1996).
39. G. Kresse, J. Furthmüller, Efficiency of ab-initio total energy calculations for metals and semiconductors using a plane-wave basis set. *Comput. Mater. Sci.* **6**, 15–50 (1996).
40. G. Kresse, D. Joubert, From ultrasoft pseudopotentials to the projector augmented-wave method. *Phys. Rev. B* **59**, 1758 (1999).
41. J. P. Perdew, K. Burke, M. Ernzerhof, Generalized gradient approximation made simple. *Phys. Rev. Lett.* **77**, 3865 (1996).
42. S. Grimme, J. Antony, S. Ehrlich, H. Krieg, A consistent and accurate *ab initio* parametrization of density functional dispersion correction (DFT-D) for the 94 elements H-Pu. *J. Chem. Phys.* **132**, 154104 (2010).
43. H. J. Monkhorst, J. D. Pack, Special points for Brillouin-zone integrations. *Phys. Rev. B* **13**, 5188 (1976).
44. S. Plimpton, Fast parallel algorithms for short-range molecular dynamics. *J. Comput. Phys.* **117**, 1–19 (1995).
45. J. M. Wang, R. M. Wolf, J. W. Caldwell, P. A. Kollman, D. A. Case, Development and testing of a general amber force field. *J. Comput. Chem.* **25**, 1157–1174 (2004).
46. B. Beck, T. Clark, R. C. Glen, VESPA: A new, fast approach to electrostatic potential-derived atomic charges from semiempirical methods. *J. Comput. Chem.* **18**, 744–756 (1997).
47. A. Mattoni, A. Filippetti, M. I. Saba, P. Delugas, Methylammonium rotational dynamics in lead halide perovskite by classical molecular dynamics: The role of temperature. *J. Phys. Chem. C* **119**, 17421–17428 (2015).
48. B. Li, Y. Kawakita, Y. Liu, M. Wang, M. Matsuura, K. Shibata, S. Ohira-Kawamura, T. Yamada, S. Lin, K. Nakajima, S. Liu, Polar rotor scattering as atomic-level origin of low mobility and thermal conductivity of perovskite $CH_3NH_3PbI_3$. *Nat. Commun.* **8**, 16086 (2017).
49. C. B. Cui, H. G. Beom, Molecular dynamics simulations of edge cracks in copper and aluminum single crystals. *Mater. Sci. Eng. A* **609**, 102–109 (2014).
50. T. Botari, E. Perim, P. A. S. Autreto, A. C. T. van Duin, R. Paupitz, D. S. Galvao, Mechanical properties and fracture dynamics of silicene membranes. *Phys. Chem. Chem. Phys.* **16**, 19417–19423 (2014).
51. D. Wang, J. Lee, K. Holland, T. Bibby, S. Beaudoin, T. Cale, Von mises stress in chemical-mechanical polishing processes. *J. Electrochem. Soc.* **144**, 1121–1127 (1997).
52. A. Stukowski, Visualization and analysis of atomistic simulation data with OVITO—The open visualization tool. *Model. Simul. Mater. Sci.* **18**, 015012 (2010).
53. COMSOL AB, COMSOL Multiphysics® v. 5.5;cn.comsol.com.
54. K. Zhang, R. Song, J. Qi, Z. Zhang, Z. Zhang, C. Yu, K. Li, Z. Zhang, B. Li, Colossal barocaloric effect in carboranes as a performance tradeoff. *Adv. Funct. Mater.* **32**, 2112622 (2022).
55. J. S. Gardner, G. Ehlers, A. Faraone, V. G. Sakai, High-resolution neutron spectroscopy using backscattering and neutron spin-echo spectrometers in soft and hard condensed matter. *Nat. Rev. Phys.* **2**, 103–116 (2020).
56. M. Bée, *Quasielastic Neutron Scattering Principles and Applications in Solid State Chemistry, Biology and Materials Science* (IOP, 1988).
57. K. Sköld, Effects of molecular reorientation in solid methane on the quasielastic scattering of thermal neutrons. *J. Chem. Phys.* **49**, 2443 (1968).
58. J. J. Rush, L. A. de Graaf, R. C. Livingston, Neutron scattering investigation of the rotational dynamics and phase transitions in sodium and cesium hydrosulfides. *J. Chem. Phys.* **58**, 3439 (1973).
59. N. Verdal, T. J. Udovic, J. J. Rush, A. V. Skripov, Quasielastic neutron scattering study of tetrahydroborate anion dynamical perturbations in sodium borohydride due to partial halide anion substitution. *J. Alloys Compd.* **645**, S513–S517 (2015).
60. J. P. Embs, E. Juranyi, R. Hempelmann, Introduction to quasielastic neutron scattering. *Z. Phys. Chem.* **224**, 5–32 (2010).


**Acknowledgments:** We acknowledge the beam time provided by SPring-8 (proposal no. 2019A2052), CSNS (proposal no. P1819062700003), ANSTO (proposal no. 7867), and BSRF. We also acknowledge the excellent support from A. Shumack and R. White of the Sample Environment Group at ANSTO for getting approval on using a high-pressure cell and subsequently setting up the high-pressure equipment on the Pelican instrument. **Funding:** This work was supported by Ministry of Science and Technology of China grants 2022YFE0109900 and 2021YFB3501201 (B.L.) and 2016YFA0401503 (B.Y.); Key Research Program of Frontier Sciences of Chinese Academy of Sciences grant ZDBS-LY-JSC002 (B.L.); International Partner Program of Chinese Academy of Sciences grant 174321KYSB20200008 (B.L.); CSNS Consortium on High-performance Materials of Chinese Academy of Sciences grant (B.L.); IMRCAS Instrument Development Program (B.L.); Young Innovation Talent Program of Shenyang grant RC210435 (B.L.); and National Natural Science Foundation of China grants 11934007 (B.L.), 52276076 (S.L.), and 22022101 and 21771011 (K.L.). **Author contributions:** Conceptualization: B.L. Data curation: D.Y., S.K., L.H., J.C., Y.W., K.L., Zhao Zhang, R.S., J.W., C.Y., Z.C., J.Y., S.L., X.L., K.Q., M.W., and R.M. Formal analysis: Y.W., K.L., S.L., and Zhe Zhang. Funding acquisition: B.L. Investigation: D.Y., Y.W., K.L., S.L., and Zhe Zhang. Methodology: D.Y., R.S., C.Z., and S.L. Project administration: B.L., S.L., K.L., and B.Y. Resources: Q.R., B.Y., and X.T. Supervision: Zhidong Zhang, B.L., K.L., and S.L. Validation: B.L., S.L., and K.L. Visualization: K.L., R.S., J.W., Z.C., J.Y., K.Q., M.W., and Zhe Zhang. Writing—original draft: Zhe Zhang. Writing—review and editing: K.L., S.L., Zhidong Zhang, and B.L. **Competing interests:** The authors declare no competing interests. A Chinese patent was filed partly on this study on 30 November 2020 by B.L., Zhidong Zhang, and Zhe Zhang and approved on 10 December 2021 with the patent number ZL202011370421.5. **Data and materials availability:** All data needed to evaluate the conclusions in the paper are present in the paper and/or the Supplementary Materials.

Submitted 16 May 2022
Accepted 13 January 2023
Published 17 February 2023
10.1126/sciadv.add0374